

Antimicrobial Peptide Mechanism Studied by Scattering-Guided Molecular Dynamics Simulation

Robert Allsopp, Anna Pavlova, Tyler Cline, Aria M. Salyapongse, Richard E. Gillilan, Y. Peter Di, Berthony Deslouches, Jeffery B. Klauda,* James C. Gumbart,* and Stephanie Tristram-Nagle*



Cite This: *J. Phys. Chem. B* 2022, 126, 6922–6935



Read Online

ACCESS |



Metrics & More

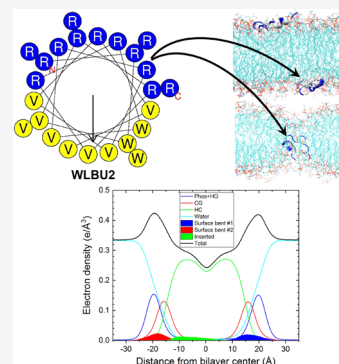


Article Recommendations



Supporting Information

ABSTRACT: In an effort to combat rising antimicrobial resistance, our labs have rationally designed cationic, helical, amphipathic antimicrobial peptides (AMPs) as alternatives to traditional antibiotics since AMPs incur bacterial resistance in weeks, rather than days. One highly positively charged AMP, WLBU2 (+13e), (RRWV RRVR RWVR RVVR VVRR WVRR), has been shown to be effective in killing both Gram-negative (G(-)) and Gram-positive (G(+)) bacteria by directly perturbing the bacterial membrane nonspecifically. Previously, we used two equilibrium experimental methods: synchrotron X-ray diffuse scattering (XDS) providing lipid membrane thickness and neutron reflectometry (NR) providing WLBU2 depth of penetration into three lipid model membranes (LMMs). The purpose of the present study is to use the results from the scattering experiments to guide molecular dynamics (MD) simulations to investigate the detailed biophysics of the interactions of WLBU2 with LMMs of Gram-negative outer and inner membranes, and Gram-positive cell membranes, to elucidate the mechanisms of bacterial killing. Instead of coarse-graining, backmapping, or simulating without bias for several microseconds, all-atom (AA) simulations were guided by the experimental results and then equilibrated for $\sim 0.5 \mu\text{s}$. Multiple replicas of the inserted peptide were run to probe stability and reach a combined time of at least $1.2 \mu\text{s}$ for G(-) and also $2.0 \mu\text{s}$ for G(+). The simulations with experimental comparisons help rule out certain structures and orientations and propose the most likely set of structures, orientations, and effects on the membrane. The simulations revealed that water, phosphates, and ions enter the hydrocarbon core when WLBU2 is positioned there. For an inserted peptide, the three types of amino acids, arginine, tryptophan, and valine (R, W, V), are arranged with the 13 Rs extending from the hydrocarbon core to the phosphate group, Ws are located at the interface, and Vs are more centrally located. For a surface state, R, W, and V are positioned relative to the bilayer interface as expected from their hydrophobicities, with Rs closest to the phosphate group, Ws close to the interface, and Vs in between. G(-) and G(+) LMMs are thinned $\sim 1 \text{ \AA}$ by the addition of WLBU2. Our results suggest a dual anchoring mechanism for WLBU2 both in the headgroup and in the hydrocarbon region that promotes a defect region where water and ions can flow across the slightly thinned bacterial cell membrane.



INTRODUCTION

While traditional antibiotics have long provided protection against bacterial infection and have allowed surgical interventions to save lives, the worldwide problem of bacterial resistance¹ continues to motivate many researchers to explore alternatives. A comprehensive report aimed at assessing rising antimicrobial resistance has predicted that by 2050, over 10 million deaths will occur annually as a result of antimicrobial-resistant pathogens.² One approach to solving this problem is to use rational design to synthesize antimicrobial peptides (AMPs) as an alternative antibiotic because bacterial resistance is slower to develop. The Montelaro/Deslouches groups were inspired by the human cathelicidin, LL-37, a helical, broad-spectrum amphipathic peptide of 37 amino acids with 12 positively charged residues.^{3,4} A second inspiration was the naturally occurring AMP on the extreme end of the C-terminal tail of the HIV-1 fusion protein, LLP1, which is also highly cationic, containing seven positively charged residues out of 28 residues.⁵

The highly cationic nature of these peptides is thought to impart selectivity toward negatively charged prokaryotic bacterial cells and lower their toxicity to host eukaryotic cells.⁶ The Deslouches lab has attempted to discover key aspects of AMP-caused bacterial killing by synthesizing simplified AMPs containing only three types of amino acids: valine (V), tryptophan (W), and arginine (R),^{4,7–10} instead of 15 types as in LL-37 or 11 types as in LLP1. By limiting the number of types of amino acids, we can better determine precisely which physical properties, hydrophobicity, hydrophobic moment, length, and charge of peptides are essential for permeabilizing cells and

Received: May 9, 2022

Revised: July 21, 2022

Published: September 6, 2022



killing bacteria. For the present work, we have focused on the rationally designed, cationic AMP WLBU2,^{11–14} which is now in Phase II clinical trials for wound healing.¹⁵

The primary structure of WLBU2 is **RRWV RRRV RWVR RVVR VVRR WVRR**, with 13 R residues (shown in bold type) out of 24 total amino acid residues. If WLBU2 were perfectly α -helical, the helical wheel design would predict that the Rs line the hydrophilic face, while the Vs line the hydrophobic face toward the lipid chains, with the Ws close to the interface between these two faces (Figure 1). W was added since it

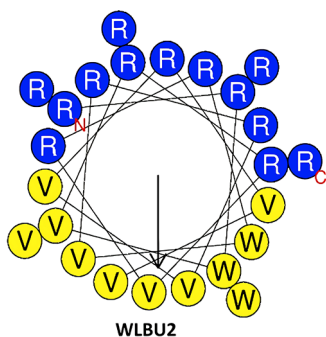


Figure 1. Helical wheel diagram of WLBU2 prepared using the Heliquest WEBSITE (heliquest.ipmc.cnrs.fr). The arrow shows the direction of the hydrophobic moment, μH .

stabilizes the AMP in saline conditions, such as in the human body.¹³ The detailed secondary structure of WLBU2 in four different lipid model membranes (LMMs) and in aqueous solution was obtained using circular dichroism spectroscopy and was published previously.¹⁶ While WLBU2 in water or 15 mM phosphate-buffered saline (PBS) adopts primarily a random coil or β -sheet structure, the α helical content increases to $\sim 80\%$ in Gram-negative ($G(-)$) inner membrane (IM) or Gram-positive ($G(+)$) LMMs and to $\sim 40\%$ in lipopolysaccharide (LPS)-containing LMMs. Although WLBU2 is not 100% helical by our determination,¹⁶ it is still primarily helical when in contact with the inner membrane of $G(-)$ and $G(+)$ LMMs, partially confirming the locations of R and V on opposite faces in WLBU2's helical wheel rational design. When added to a eukaryotic membrane mimic, we found only a low level of α -helicity ($\sim 20\%$).¹⁶ Thus, the secondary structure of WLBU2 plays an important role in its ability to avoid toxicity to host eukaryotic cells while remaining toxic to prokaryotic bacterial cells.

For the current study, we implement molecular dynamics (MD) simulations to visualize the orientations of WLBU2 when interacting with four different bacterial LMMs. By constraining the thickness of the different LMMs to those obtained using X-ray diffuse scattering (XDS), and the locations of the peptide to those obtained using neutron reflectometry (NR), a starting point for the simulation is obtained. Then, by simulating for an additional ~ 0.5 microseconds, the conformations of WLBU2 and the surrounding lipids are allowed to equilibrate to the final membrane-peptide structure and an electron density profile (EDP) is produced. Fourier transformation of the EDP produces a continuous form factor ($F(q_z)$). By comparing the simulated $F(q_z)$ with the experimental $F(q_z)$ obtained using X-ray diffuse scattering (XDS), the simulation's accuracy is determined. This comparison anchors the all-atom (AA) MD simulation to the experimentally determined lipid thickness and structure. We show simulation/experimental comparisons for

four LMMs that mimic the outer (LPS and KDO2) and inner $G(-)$ membranes and the $G(+)$ cell membrane. The LMMs are constructed of mixtures of pure lipids that mimic the lipid composition of bacterial cells.¹⁷ Previously published results for KDO2 simulations, NR peptide locations, and XDS form factors are provided in the SI for convenience and briefly described in the Results section since these results are essential for comparison to the present simulation work. Molecular details of WLBU2's conformation in the membrane give insights into the mechanism of bacterial killing by WLBU2's membrane perturbation.

MATERIALS AND METHODS

MD Simulations. KDO2. The KDO2 simulations were previously published in ref 16. For convenience, these methods and results are found in the SI and in Figure S1.

$G(-)$ Inner Membrane (IM). Each simulation involved membranes with lipids that were composed of POPE/POPG/TOCL in a 7:2:1 molar ratio, as in the scattering experiments.¹⁶ Each simulation had either one or two peptides that were placed in different locations, with either 100 or 160 total lipids. The simulations were created using 45–60 TIP3P waters per lipid¹⁸ and 27–38 K^+ ions depending on the size of the simulation. Simulations were run on the Extreme Science and Engineering Discovery Environment (XSEDE) using the Texas Advanced Computing Cluster (TACC) on Stampede2 and also on Comet and Expanse at the San Diego Supercomputer Center at U.C. San Diego. The simulations were run for 300 ns for the surface simulations and at least 420 ns for the inserted simulations to probe stability. It was known from the beginning that the peptide easily comes out of the membrane and that it was a challenge to sustain the peptide inside the membrane. Peptides remained in the membrane when surface tension was applied and the structure agreed better with the experiment. The need for adding additional surface tension likely arose from small inaccuracies in the force field (lipid–lipid and protein–lipid interactions).¹⁹ Additional details concerning the stability of the inserted peptide position are given in the SI (see Figures S2 and S3).

The peptide was not locally restrained for the $G(-)$ trials. The only bias was the use of additional surface tension that was later adjusted and reduced to finally optimize the fit by taking the last 100 ns for analysis. The initial location and number of peptides were varied, as was the surface tension (from 0 to 15 dyne/cm). All surface simulations were run with NPT (isothermal–isobaric) or NP γ T (isothermal–isobaric with lateral surface tension). The calculated form factors (see below) were used as a measure of success for the different simulations, focusing on the cross-over points (zero positions) on the x-axis and relative lobe intensities and their comparison to the XDS experiment. Additional details concerning the stability of the inserted peptide position are given in the SI (see Figures S2 and S3).

To reduce the system size, unwanted interactions, and complexity, the peptides were simulated separately in two states (surface-bound or inserted). The surface tension applied for the surface-bound or inserted states of WLBU2 differed because the initial optimization of the inserted peptide incurred large errors in certain regions of low q -space when the surface tension was the same as the surface-bound state. There are several surface tension combinations that matched the form factor crossing points (see below), but the best combination to lower the sum squared error was 9 dyne/cm for the surface-bound and 15 dyne/cm for the inserted WLBU2.

MD simulations of G(−) membranes utilized NAMD 2.12–2.14 depending on the resource,²⁰ while also using the CHARMM36 force field for lipids²¹ and CHARMM36m force field for proteins.²² A 2 fs time step was employed with long-range electrostatics interactions evaluated every other time step using the particle mesh Ewald method.²³ Short-range non-bonded interactions were cut off at 12 Å using a force-based switching function beginning at 10 Å. The temperature was maintained at 37 °C using Langevin dynamics, and pressure was maintained separately in the membrane-planar (when no surface tension was applied) and membrane-orthogonal direction using a Langevin piston at 1 atm.

G(+) Membrane. The G(+) membrane model was comprised of POPG/POPE/DOTAP/TOCL in a 6:1.5:1.5:1 molar ratio, which has one protonated phosphate group and charge $-1e$, equally distributed between the two leaflets, for a total of 80 lipids. A total of 5665 TIP3P water molecules and 44 Na⁺ ions were added. The system was run for 300 ns. The system was also run for 300 ns under an applied surface tension of 9 dyne/cm. The simulations were carried out at 37 °C.

The WLBU2 peptide was added to the surface of the G(+) membrane in the straight and bent conformations (see Robetta modeling below). Each system was run for 400 ns under an applied surface tension of 9 dyne/cm; the last 100 ns was used for analysis. For comparison, an additional simulation of an alternative bent surface conformation was run for 400 ns equilibration and 400 ns with 9 dyne/cm applied. A model with the peptide inserted in the center of the membrane was also simulated. To stabilize the WLBU2 peptide at the center of the membrane, Tcl boundary forces in NAMD were used to create space by slowly pushing the lipids outward over the course of ~20 ns. Once there was enough space for the peptide, it was inserted and then held fixed for 150 ns while lipids equilibrated around it. Water was also prevented from going into the membrane during this process. The inserted model was then run under no surface tension for 100 ns, followed by 15 dyne/cm surface tension for 200 ns with the peptide restrained, and then 200 ns with no peptide restraint. All simulation parameters were the same as those used for the G(−) membrane, although NAMD 3 on GPUs was used for some runs.²⁰ Additional details concerning the stability of the inserted peptide position are given in the SI (see Figure S4).

LPS Membrane. The symmetric pure LPS membrane was a mixture of 24 *P. aeruginosa* Type 1 (six acyl chains) and 48 Type 2 (five acyl chains) LPS equally distributed between the two leaflets. The lipid/peptide molar ratio was 72:1, close to the XDS lipid/peptide molar ratio of 75:1. Each LPS molecule was capped with 10 core 1b sugars and had a charge of $-10e$. The membrane was built using CHARMM-GUI^{24,25} and was solvated above and below with 15269 total TIP3P water molecules and 720 Na⁺ ions to neutralize the system. Because the phosphate group on LPS may be protonated,²⁶ we modeled both the fully deprotonated ($-10e$) and singly protonated on each phosphate ($-8e$) LPS, with the latter having a corresponding reduction in Na⁺ ions. The systems were equilibrated for 200 ns with the last 100 ns used for analysis. The other simulation details are the same as for the G(+) membrane, including the system with WLBU2 in the center of the membrane.

Electron Density Profiles (EDPs) from Simulation. Simulated form factors were produced from the computer-generated “SIM” file, which identifies all atoms and their positions in the bilayer, using the SimtoExp software.²⁷ EDPs, which are the

Fourier transform of the form factors, were also produced using the SimtoExp software. The SimtoExp software finds chi-square goodness of fit between the experimental and simulated form factors.

Robetta Modeling. An initial protein starting structure is required for simulations. For this, the Robetta^{28,29} server was utilized. Robetta is an online protein prediction server developed by the Baker Laboratory at the University of Washington. Robetta uses the Ginzbu prediction protocol to match protein chains into putative domains with reasonable confidence. The structure and 3-D models are constructed using homology modeling with comparisons made to proteins with solved structures and *ab initio* structure prediction methods designed by the Robetta server. Robetta returned with confidence two distinct models for WLBU2. Since both models (see Figure 2a,b) were predicted with confidence using the Robetta server,

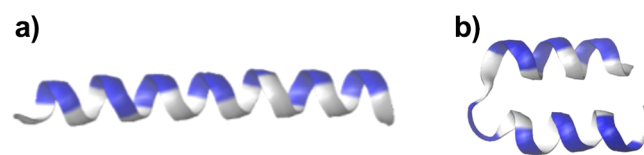


Figure 2. Structural predictions from the Robetta software. (a) Straight helix. (b) Bent helix. Colors: R, blue; W, V, white.

both were considered potential starting structures for the simulations in this work. However, the bent helix conformed better to the secondary structure obtained using circular dichroism (CD).¹⁶ During the simulations, the helical secondary structure was not constrained. Additional details concerning the Robetta modeling are given in the SI.

X-ray Diffuse Scattering (XDS) and Neutron Reflectivity (NR). No new NR data were obtained for the present work; the NR materials and methods and results were previously published in the SI in ref 16 and are reproduced in the SI for convenience. While most of the XDS data were previously published in ref 16, additional XDS were obtained of the G(−) control for the purpose of assessing the reproducibility of the experimental form factors. For this comparison, G(−) control data were obtained on two virtual CHESSE runs, where the sample substrate was varied as was the method of data collection, and compared to CHESSE data collected in 2018. In 2018, samples were deposited onto flat silicon wafers, which were rotated to X-ray all of the angles equally, using a motorized internal rotation within the hydration chamber. In November 2020, samples were deposited onto highly polished, cut quartz glass rods of radius 9 mm that were not rotated in the beam. In June 2021, samples were deposited onto flat silicon wafers, which were rotated using a large rotation motor, external to the chamber. The XDS methods from ref 16 are reproduced in the SI for convenience. A previously unpublished image of XDS for G(−) control is shown as an example of X-ray diffuse scattering in Figure 3.

RESULTS

Neutron Reflectivity (NR). NR informs about the location of WLBU2 in the membrane. This is a key metric for the accuracy of the MD simulations since it constrains them to consider an internal location in the hydrocarbon region. Since this AMP, WLBU2, is highly cationic ($+13e$), it is not intuitive that it would locate in the hydrocarbon region. Nevertheless, the NR showed two possible locations for WLBU2, in the

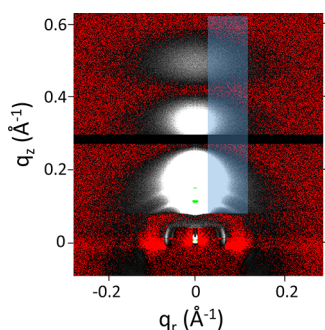


Figure 3. $G(-)$ IM control. A 2D image collected at CHESSE at 37 °C using the Eiger 4M hybrid detector in November 2020. The sample was oriented onto a cut, quartz glass rod. The intensity in white lobes underneath the blue swath provides the intensity data for the form factor data to compare to MD simulation. Green spots correspond to lamellar orders, $n = 3$ and 4. The black horizontal line at $q_z \approx 0.3 \text{ \AA}^{-1}$ is due to the separation between panels in the Eiger 4 M detector.

headgroup and in the hydrocarbon region (Figure S5). The dual location is the case for both $G(-)$ inner membrane (Figure S5b) and $G(+)$ (Figure S5c) membrane mimics. For KDO2, the data in Figure S5a show that WLBU2 locates only in the headgroup region, whereas for LPS, WLBU2 is located only in the hydrocarbon region in Figure S5d. Figure S5 was previously published in ref 16 and is reproduced in the SI since it is relevant for the present work. The MD simulations in the present work used these peptide locations from NR in different lipid model membranes.

XDS Form Factors. As described in the SI and shown in Figure S6, the XDS intensity gets converted into a form factor, which is the first step in comparing to the form factor obtained from MD simulation. The sharp minima in Figure S6 at $|F(q_z)| = 0 \text{ e/\AA}^2$ are related to the thickness of the membrane. If these minima (also known as cross-over or zero points) move in $q_z (\text{\AA}^{-1})$ to larger values, this indicates that the membrane thins. Thus, we can compare directly the form factors generated from the MD simulation with the experimental form factors to ascertain if the membrane thickness is the same. In this work, we further investigated the reproducibility of the X-ray data minima at $q_z \approx 0.26 \text{ \AA}^{-1}$ and $q_z \approx 0.40 \text{ \AA}^{-1}$ by making many scans of $G(-)$ IM control on two different substrates (silicon wafers and

cut glass rods). As shown in Figure 4a, there is little variability in the cross-over points between different samples. This indicates that despite using two different substrates, three different sample-to-detector distances, three different wavelengths at CHESSE, and three different methods of data collection, when pixels are converted to q_z values, there is a surprisingly good agreement. There is some variability in the ratio of amplitudes, which is attributed to inhomogeneities in the sample thickness. This inhomogeneity was more apparent in the samples prepared on cut glass rods where the Rock and Roll procedure is problematic due to the cylindrical geometry. Cut glass rods were used in one virtual run at CHESSE (see Figure 3), in place of rotating a flat sample from -1.6 to 7° during the data collection. For comparison, in Figure 4b, the 2018 $G(-)$ control data are overlaid on the concatenated 13 scans shown in Figure 4a.

Comparison of Experimental and Simulated Form Factors. **KDO2.** Figure S1 shows the MD simulation and experimental results for KDO2. In Figure S1a, the form factor that results from the MD simulation is directly compared to that from the XDS experiment for pure KDO2. As shown, there is remarkable agreement between the experimental and simulated form factors, especially the positions of the cross-over points, verifying that the force field and sampling used in the simulation accurately reproduce the equilibrium membrane structure and that no surface tension is required. Figure S1b shows the EDP produced from the simulation results using the SimtoExp computer program, and Figure S1c shows a visualization of the KDO2 simulation, prepared using Visual Molecular Dynamics (VMD). Figure S1d shows the comparison of form factors for the case where WLBU2 was added to KDO2 (72:1 lipid/peptide molar ratio). In Figure S1e, the EDP shows the location of WLBU2 in the outer headgroup region of KDO2, outside of the octulosonic acid residues. This is shown visually in Figure S1f, where WLBU2 was initially constrained as a bent α -helix since our circular dichroism results found it to be 67% helical in KDO2.¹⁶ When all constraints were removed, WLBU2 remained primarily helical. See the Materials and Methods section for the rationale for using a bent or a straight WLBU2.

$G(-)$ Inner Membrane (IM). Initial efforts to simulate the control $G(-)$ IM model membrane were carried out without a surface tension applied, as with KDO2 (Figure S1). Three replicas of an all-atom membrane were constructed using

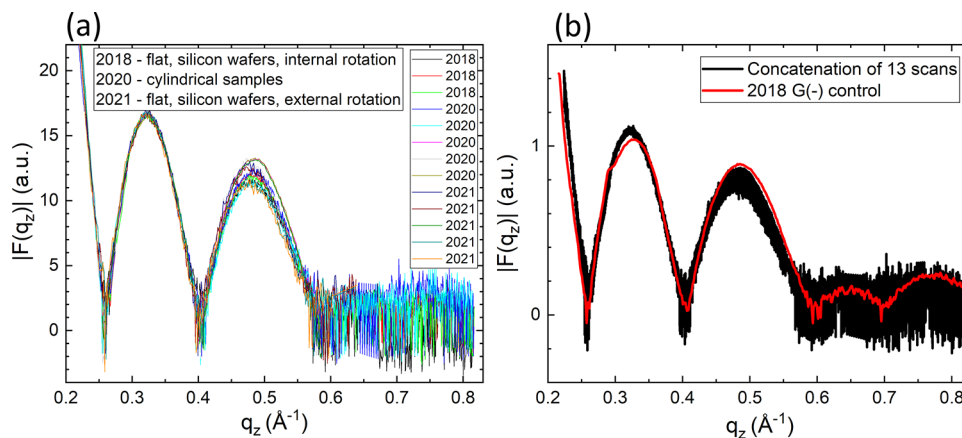


Figure 4. (a) Form factor data for $G(-)$ IM LMM control (POPE/POPG/TOCL 7:2:1 molar ratio) obtained at CHESSE at 37 °C on cut glass rods or on flat, highly polished silicon wafers that were rotated either externally or internally during data collection (see legend). Amplitudes were normalized in the first, full lobe. Data collected in 2020 and 2021 have not been previously published. (b) Concatenated scans in 4(a) overlaid with $G(-)$ control data from 2018, which was used to compare to MD simulation.

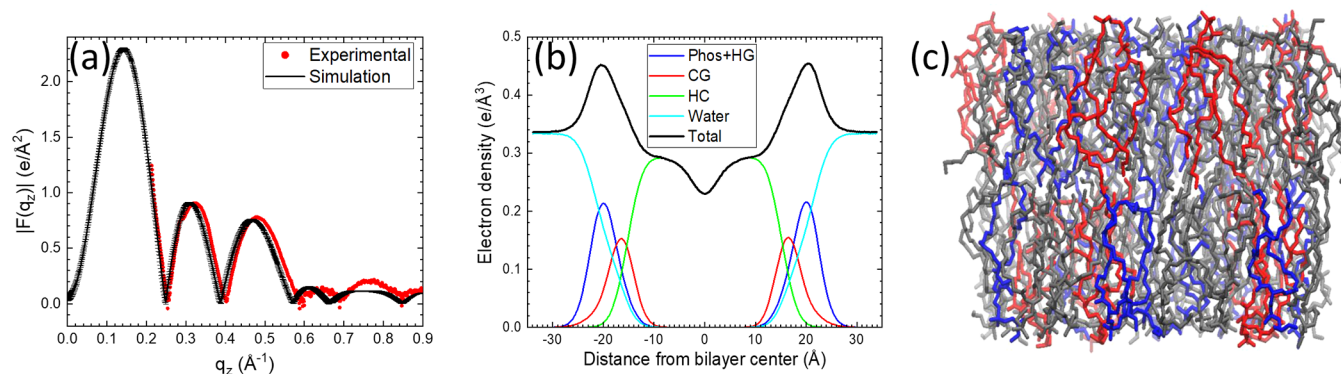


Figure 5. (a) Unsuccessful attempt to match the form factor for G(−) IM simulated without surface tension (black line) and the experimental form factor (red circles). The simulated form factor data are shown as an average of 3 simulations, with standard deviations. (b) Simulated EDP. Colors: Total, black; phosphate + outer headgroup, blue; carbonyl–glycerol, red; hydrocarbon, green; and water, cyan. (c) VMD visualization of the simulated G(−) IM bilayer. Colors: POPE, gray; POPG, blue; and TOCL, red.

CHARMM-GUI's Membrane Builder.^{21,25,30,31} The results of this simulation of control G(−) IM are shown in Figure 5. In Figure 5a, the agreement between the simulated form factor (black) and experimental form factor (red) is suboptimal. While the amplitudes of the diffuse lobes match fairly closely, places where $F(q_z)$ go to zero (the cross-over points) are not in good agreement. This comparison indicates that the simulated bilayer is thicker than that of the experimental data. Figure 5b shows the simulated EDP and Figure 5c shows the VMD visualization.

In an attempt to match more closely to the experimental bilayer thickness, various small surface tensions were applied and simulated between 9 and 15 dyne/cm. This resulted in shifting the positions of the zeroes (cross-over points). The best agreement with the experimental form factor for the control G(−) IM LMM was observed when a surface tension of 9 dyne/cm was applied (Figure 6a). Figure 6b shows the simulated EDP and Figure 6c shows the VMD visualization of control G(−) IM LMM. The inclusion of potassium ions caused no change to the goodness of fit to the experimental data due to the ~ 15 times smaller amount compared to the sodium ions in KDO2.

When WLBU2 was added to the G(−) membrane mimic, the best agreement with the experiment was obtained when the peptide simulated density was split into both a bent surface model at 9 dyne/cm and a bent inserted model at 15 dyne/cm (see Table 1). The weighting of the surface and inserted models was constrained to 37.2% inserted and 62.8% surface (see Figure S7a) based on fitting the NR result to two Gaussians (Figure S5b). Note that significant oxygen atoms from the glycerol–carbonyl, phosphate headgroups, and water enter the bilayer interior in Figure 6g. Table 1 shows the sum of squares errors for different WLBU2 locations and surface tensions. Note that this procedure of dividing the peptide density into surface and inserted assumes that there is no interaction between the surface and inserted states of WLBU2, as we have previously performed in the case of the lung surfactant proteins SP-B and SP-C.³² While the surface state results in Table 1 were from an MD simulation where two WLBU2s were added to the G(−) LMM (one on each side), we also performed a smaller simulation where one WLBU2 was added to only one side. There was an insignificant difference in the form factors as shown in Figure S8.

A visualization of a close-up of WLBU2 inserted into G(−) IM LMM is shown in Figure 7a. When the Rs are located in the center of the hydrocarbon region, phosphates, K^+ ions, and water are drawn into the membrane. Figure 7b shows that there is a significant electron density of water in the center of the

Table 1. Sum of Squares Error (SSE) for Different G(−) IM/WLBU2 Simulations at 37 °C^a

	1st lobe	2nd lobe	3rd lobe	total SSE (lobes + zeroes)
combined ^b (shown in Figure 6d,e)	0.53	0.16	1.00	3.07
bent inserted 0 dyne/cm	1.36	6.71	10.04	19.72
bent inserted 15 dyne/cm	1.04	1.74	1.60	5.66
bent surface 0 dyne/cm	0.74	1.75	2.52	6.70
bent surface 9 dyne/cm	0.37	0.18	1.13	3.13
straight surface 0 dyne/cm	0.66	1.32	1.38	4.86
straight surface 9 dyne/cm	0.39	0.20	1.34	3.52

^aThe amplitudes of the three diffuse lobes in the experimental form factor were compared to the amplitudes of the simulated form factors. SSE of each lobe was computed along with the total SSE of the entire curve, as described in the Materials and Methods section. ^bSurface tension of the combined model: 15 dyne/cm for the bent inserted WLBU2 and 9 dyne/cm for the bent surface WLBU2. The above simulation was carried out at a G(−)/WLBU2 molar ratio of 87:1; a second simulation at a molar ratio of 80:1 produced similar errors.

bilayer in the case of inserted WLBU2 but not for the two surface states of WLBU2.

The MD simulation gives information about the location of the three types of amino acids across the bilayer. To see these visually, we have plotted the groupings of R, W, and V in Figure 8. These amino acid locations were obtained directly from the MD simulation, using the SimtoExp program, which calculates density in 0.5 Å slices through the bilayer thickness.^{27,33} For the two surface models, R is closest to the aqueous phase, followed by V and then W, which is closest to the interface between headgroups and hydrocarbon chains (near the carbonyl–glycerol group). These locations of amino acids follow their hydrophobicity, with W the most hydrophobic.³⁴ For the inserted model, R stretches the length of the hydrocarbon core and into the glycerol–carbonyl region, while W is located near the interfacial region and V deep into the hydrocarbon region. Therefore, in the inserted model, the amino acid residues do not follow their hydrophobicities. In Figure 8b,c, the phosphate + outer headgroup and glycerol–carbonyl components from Figure 6e are superimposed on the amino acid density to visualize their relative locations.

G(+) Membrane. For G(+) LMM, good agreement occurred between simulated and experimental form factors for the control without an applied surface tension. When the peptide WLBU2

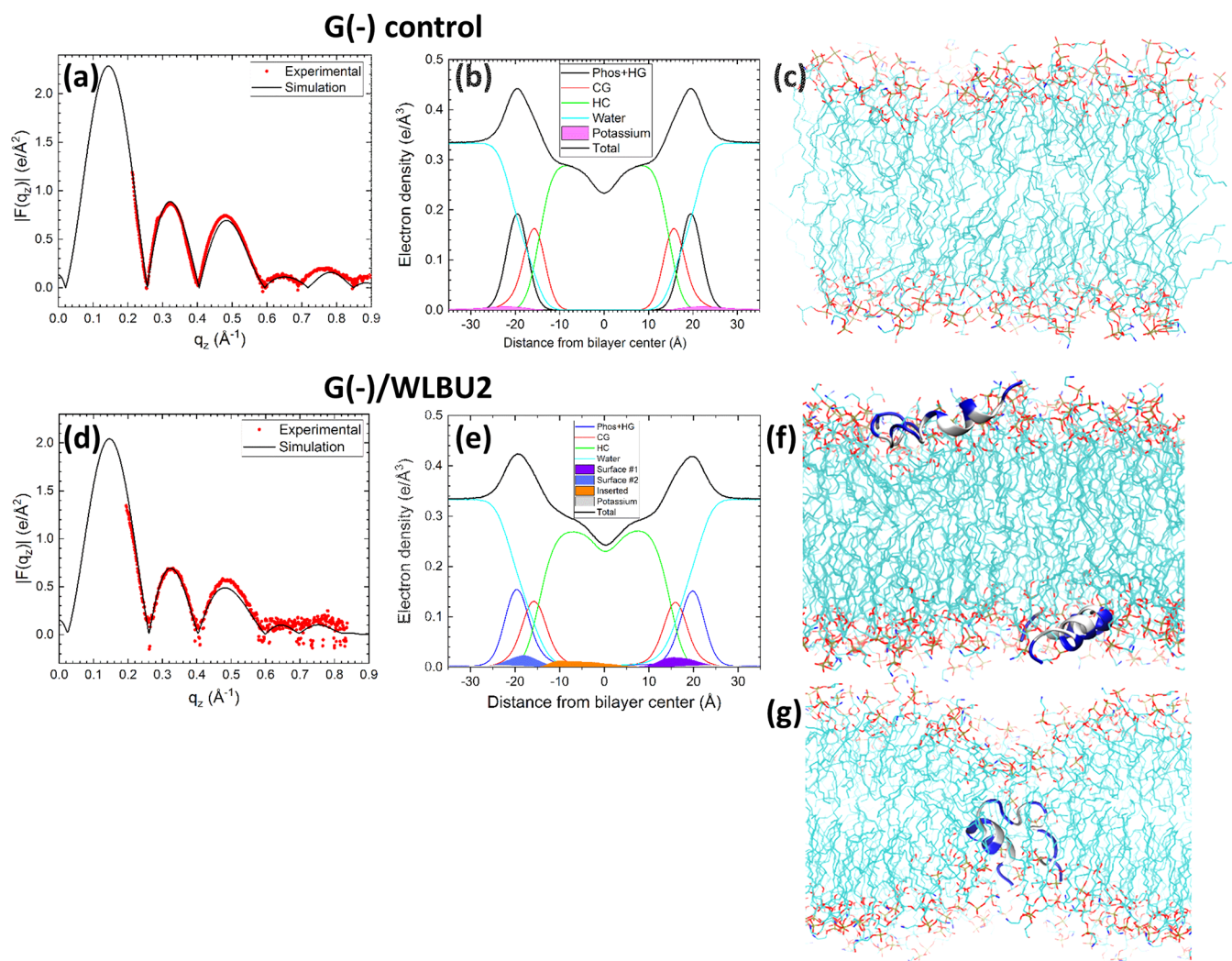


Figure 6. (a) G(-) IM control simulated (black line) and experimental form factors (red circles). (b) G(-) IM simulated EDP. Colors: Total, black; phosphate + outer headgroup, blue; carbonyl-glycerol, red; hydrocarbon, green; water, cyan; and K⁺, gray. (c) VMD visualization of G(-) IM control. Colors: Oxygen atoms, red; hydrocarbon chains, cyan. (d) G(-)/WLB2, simulated (black line) and experimental form factors (red circles). (e) G(-)/WLB2 simulated EDP. Colors: as in (b) with surface WLB2#1, filled purple; surface WLB2#2, filled blue; and inserted WLB2, filled orange. (f) VMD visualization of two surface states. Colors as in (c) with WLB2: R, blue; W,V, white. (g) VMD visualization of inserted WLB2. Colors as in 6(f).

was added to the G(+) membrane mimic, the best agreement with the experiment was obtained when the peptide simulated density was split into both a bent surface model at 9 dyne/cm and a bent inserted model at 15 dyne/cm. The goodness of fit was not affected by the presence of Na⁺ ions since their amount is $\sim 10\times$ smaller than in the KDO2 simulation. The weighting of the surface and inserted models was constrained to 54% surface and 46% inserted (see Figure S7b) based on integrating the intensity under the peaks in the NR result (Figure S5c). The results shown in Figure 9 represent the best fit of the experimental data to variations in peptide conformation, surface tension, and peptide location. The straight, surface conformation results are not shown since the agreement with the experiment was worse, as determined by the chi-square fitting in the SimtoExp program. Note that in Figure 9g, significant oxygens on the glycerol/carbonyl, phosphate, and water groups (red spheres) enter the hydrocarbon region when WLB2 is inserted near the center of the bilayer. Water and Na⁺ ions (shown in Figure 10a) are transported through the bilayer due to the internal location of WLB2.

The visualization of WLB2 inserted into the G(+) LMM is shown in Figure 10a. Like G(-) IM, the interior location of WLB2 causes water, phosphate groups, and ions to enter the hydrophobic membrane. When the water electron density is plotted (Figure 10b), it shows that significant water enters the bilayer in the combined model of WLB2 in the headgroup (54%) and in the hydrocarbon locations (46%) compared to the control. The molecular locations of the three classes of amino acids in WLB2 in the G(+) membrane mimic are shown in Figure 10c. For the surface model, R locates near the phosphate group, while W locates near the interfacial region at the carbonyl-glycerol. W is more deeply buried, as expected from its greater hydrophobicity.³⁴ For inserted WLB2, Ws lodge closer to the interface than do Vs, while Rs span the entire hydrophobic width and extend even to the phosphate group. In Figure 10, the phosphate + outer headgroup and glycerol-carbonyl components from Figure 9e are superimposed on the amino acid density to visualize their relative locations. These amino acid locations are similar to those in the G(-) IM LMM.

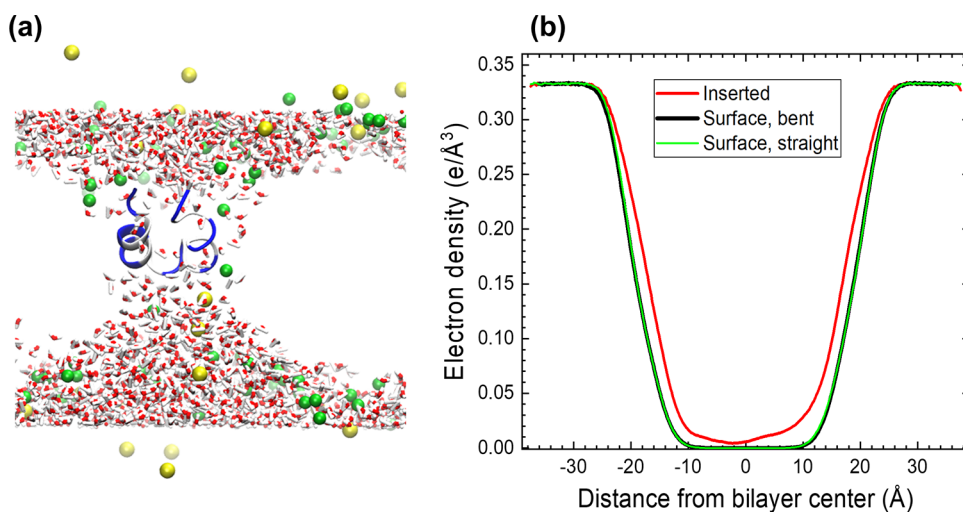


Figure 7. (a) VMD visualization of WLBU2 inserted into G(−) IM LMM. Colors: WLBU2, ribbon + licorice (R, blue; V,W, gray) K⁺ ions, yellow spheres; phosphate groups, green spheres; and water, red and white sticks. Acyl chains are omitted for clarity. (b) Water electron density of the G(−) IM bilayer with WLBU2 either inserted (red line) or on the surface in two different conformations (green and black lines (superimposed)).

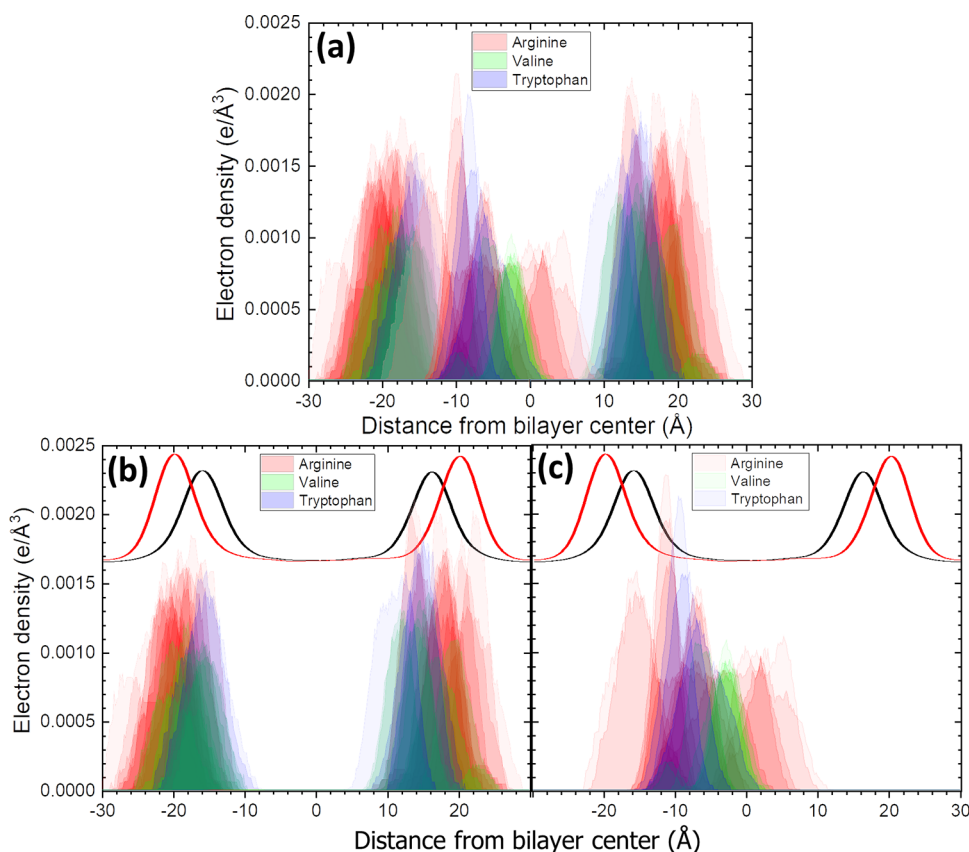


Figure 8. (a) The molecular locations relative to the bilayer center of the three types of amino acids in WLBU2 in G(−) membrane mimic. While (a) shows surface and inserted models superimposed, (b) shows the two surface models, and (c) shows the inserted model. Colors in legend. The positions of the phosphate + outer headgroup (red line) and glycerol-carbonyl (black line) are superimposed (lines not drawn to scale) on the amino acid electron density (not drawn to scale).

Lipopolysaccharide (LPS). NR indicated in Figure S5d that WLBU2 is located only in the hydrocarbon region. Therefore, WLBU2 was stable in the center of the LPS bilayer. As shown in Figure 11a, the agreement is not as good between experimental and simulated form factors as for the other LMMs, even for the control. Several simulations were attempted but were not more successful than in Figure 11a. Although our wide-angle X-ray

scattering revealed that LPS purified from PA01 is in the fluid phase at 37 °C since it lacks the sharp chain-chain correlation typical of gel phases (data not shown), this sample did not produce any diffuse X-ray scattering, even at full hydration. Therefore, we included a lipid with LPS that does fluctuate (DLPG) to obtain diffuse scattering. When the simulation was carried out with the same mixture of LPS and DLPG as in our

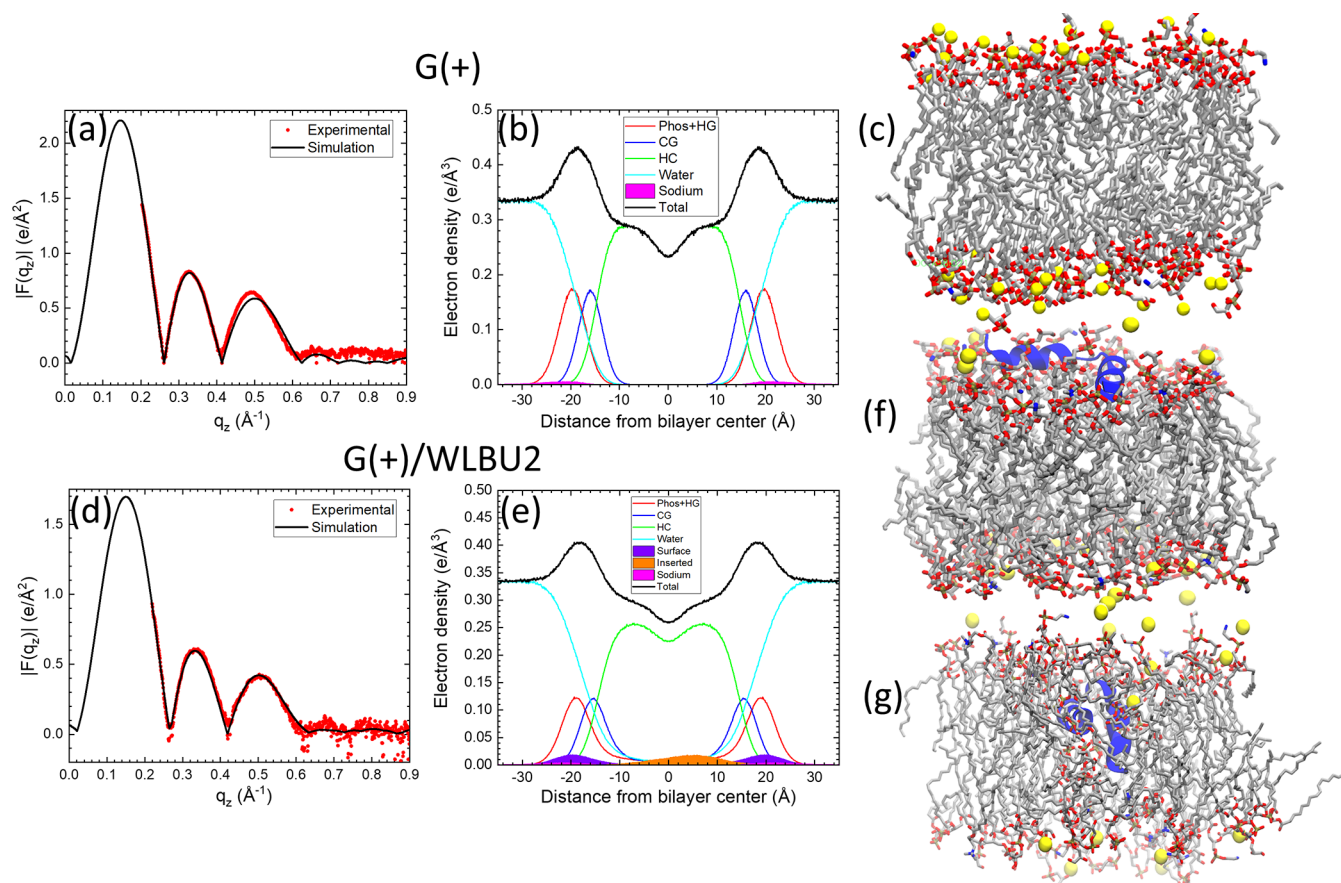


Figure 9. (a) Form factors of experimental (red circles) and simulated G(+) control (black line) at 0 dyne/cm surface tension. (b) Electron density profile of control G(+), colors in legend. (c) VMD visualization of G(+) control. Colors: carbon, gray sticks; oxygen, red sticks; and Na⁺ ions, yellow spheres. (d) Form factors of experimental data (red circles) with the combined simulated form factors G(+)/WLBU2 (black lines). (e) Combined simulated electron density profiles G(+)/WLBU2, colors in legend. Combined signifies 54% bent WLBU2 in a headgroup location at 9 dyne/cm plus 46% bent WLBU2 in a hydrocarbon location at 15 dyne/cm. (f) VMD visualization of G(+)/WLBU2 (bent, surface conformation at 9 dyne/cm). (g) VMD visualization of G(+)/WLBU2 (bent, inserted conformation at 15 dyne/cm). Colors for F and G as in C, with WLBU2 as a blue ribbon. G(+)/LMM: POPG:POPE:DOTAP:TOCL (6:1.5:1.5:1 molar ratio).

experiment (9:1 molar ratio), no better agreement was obtained than when pure LPS was simulated. The simulated results shown in Figure 11, therefore, are for pure LPS. When the simulated Na⁺ ions were included in this comparison, the agreement was worse as judged by the chi-square in the SimtoExp program and so the Na⁺ ions were not included for the same reasons as with KDO2.¹⁶ In Figure 11a,d, good agreement between experimental and simulated form factors is obtained only in the q_z region between 0.2 and 0.3 Å⁻¹. For the rest of these noisy experimental data, the zeroes, or cross-over points, are not clearly defined. However, this flattened-out form factor is clearly different from form factors for KDO2 (Figure S1a,d), suggesting that the bulky core sugar residues beyond the two octulosonic acid residues are the reason for the degradation of the X-ray form factors. The simulated form factors are degraded to a smaller extent since fewer sugar residues are used in the simulation (no O-antigens).

Figure 12 shows that significant water enters the thin, hydrocarbon core when WLBU2 is inserted into the LPS membrane. Table 2 summarizes the structural results obtained from the simulations for the four LMMs with and without WLBU2.

DISCUSSION

While MD simulation is a powerful tool to visualize molecules and measure molecular distances, equilibration of unbiased simulations to reach an equilibrated state of peptides in the membrane can require >0.8 μs.³⁵ One way to circumvent this problem is to carry out coarse-grained simulations on milli-second time scales.³⁵ Then, back-transforming (backmapping) from coarse-grained to atomistic simulation can be performed to visualize the atomistic configurations of the lipid and peptide molecules at a higher resolution.³⁶ This multiscale approach is valuable and has yielded many innovative publications.^{37–43} Another method to shorten the atomistic simulation time of adding peptides to membranes is to allow the peptide and lipids to self-assemble together into a lipid bilayer with the peptide incorporated.⁴⁴ Another method is a steered molecular dynamics simulation whereby a peptide is pulled into the membrane and allowed to equilibrate.⁴⁵ An alternative approach is to compare biased all-atom peptide simulations with peptide-membrane placement to some form of fully equilibrated experimental data. Studies have compared atomistic simulation to small-angle X-ray scattering (SAXS),⁴⁶ atomic force microscopy (AFM),⁴⁷ nuclear magnetic resonance (NMR),⁴⁸ circular dichroism (CD) and NMR,⁴⁹ analytical ultracentrifugations and ¹³C NMR,⁵⁰ sum frequency generation (SFG)

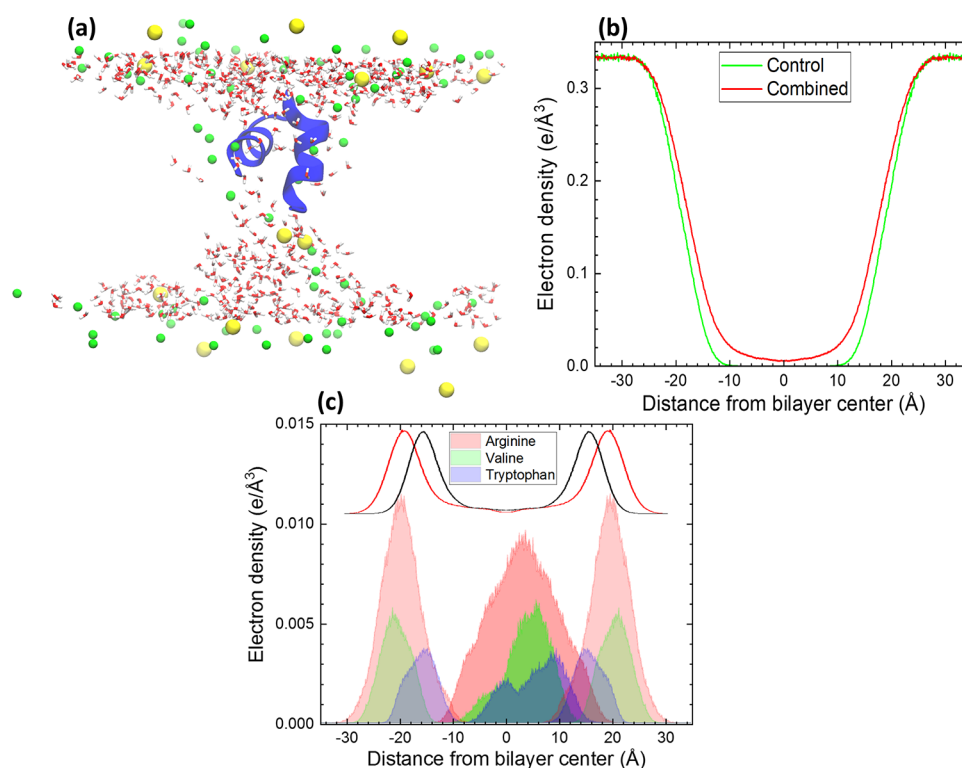


Figure 10. (a) VMD visualization of inserted WLBU2 in G(+) LMM. Colors: WLBU2, ribbon + licorice (R, blue; V,W, gray) Na⁺ ions, yellow spheres; phosphate groups, green spheres; and water, red and white sticks. Acyl chains are omitted for clarity. (b) Water electron density profile in control G(+) and in the combined model (54% HG, 46% HC) of WLBU2 in G(+) LMM. (c) Locations of all of the amino acids in WLBU2 in the bent surface and bent inserted models in the G(+) LMM. Colors in legend. The positions of the phosphate + outer headgroup (red line) and glycerol-carbonyl (black line) are superimposed (lines not drawn to scale) on the amino acid electron density (not drawn to scale).

vibrational spectroscopy and ATR-FTIR,⁵¹ fluorescence microscopy,⁵² and CD spectroscopy.⁵³ These experimental techniques can validate the percentage helical content in the peptide (CD and NMR), the amount of aggregation (analytical ultracentrifugations and ¹³C NMR), the orientation of a peptide in a membrane (SFG and ATR-FTIR), or multimer formation (SAXS and AFM).

A recent similar investigation to the present work using MD simulation and NMR spectroscopy indicates that the area per lipid (APL) increases from KDO2 (Re LPS mutant) to LPS containing six core sugar residues (Rc LPS mutant),²⁶ which is in agreement with our increase in APL from Re to LPS containing 10 core sugar residues (Ra LPS mutant) (Table 2). Similarly, both investigations observe a decrease in bilayer thickness from KDO2 to LPS, although the hydrophobic bilayer thickness reported in this work for the LPS Ra mutant is 6 Angstroms smaller than that for the Rc mutant (Figure 5 in ref 26). This difference could be related to the increased fluctuations caused by additional sugar residues, thus fluidizing the membrane.⁵⁴ Alternatively, it could be because Rice et al. used *Salmonella enterica* LPS, whereas we used *Pseudomonas aeruginosa*01 LPS. For the counterion in our MD simulation, KDO2 and LPS were both neutralized with Na⁺ ions, while in our experiment, KDO2 was neutralized with ammonium ions and PA01 LPS was neutralized with protons. In our study, APL increased for both Re LPS and Ra LPS as the lipid was protonated, thus displacing Na⁺ ions (Table 2). Our result agrees with another MD simulation that found an increase in APL as Na⁺ ions were removed from DPPC.⁵⁵ A second MD simulation of a similar 24-mer cationic AMP found an increase in APL upon the addition of AMP with a simpler lipid model

membrane,⁵⁶ in agreement with our area results shown in Table 2.

What do our results mean for the WLBU2's mechanism of action for killing bacteria? Let us consider KDO2, where NR and MD simulations locate the peptide in the headgroup region. In Figure S1f, the VMD visualization shows WLBU2 with the R residues facing downward on the surface of the KDO2 membrane. A cartoon structure of KDO2 is shown in Figure 13, depicting the charges on the octulosonic acid residues and phosphates on the mannose residues. In the MD simulation, WLBU2 was placed in the water phase above the membrane, and it then migrated toward the surface of KDO2, where it remained for the duration of the 400 ns simulation, failing to reach the phosphate groups (Figure S1e).

For WLBU2 to kill bacteria, it must translocate across the outer membrane, through the periplasmic space, and then perturb the inner membrane in G(−) bacteria. Since KDO2 is a rare, rough mutant of LPS, its AMP headgroup location may not be typical for the outer membrane of most G(−) bacteria.⁵⁷ Thus, if most bacteria had KDO2 instead of LPS in the outer leaflet of the outer membrane, we suggest that they would not be killed by WLBU2 since the AMP would not permeate further, although this experiment has not been done. We have shown previously that the abundance of carbohydrate residues in the LPS headgroup causes increased membrane fluctuations, which could facilitate peptide entry into the hydrocarbon interior.⁵⁸ For our outer membrane mimic, LPS, NR in Figure S5d indicates that WLBU2 is located only in the hydrocarbon interior. The VMD visualization of WLBU2 in LPS in Figure 11f shows the bent conformation, with ~50% α -helix, which is similar to the ~40% α -helix determined by CD.¹⁶ This interior

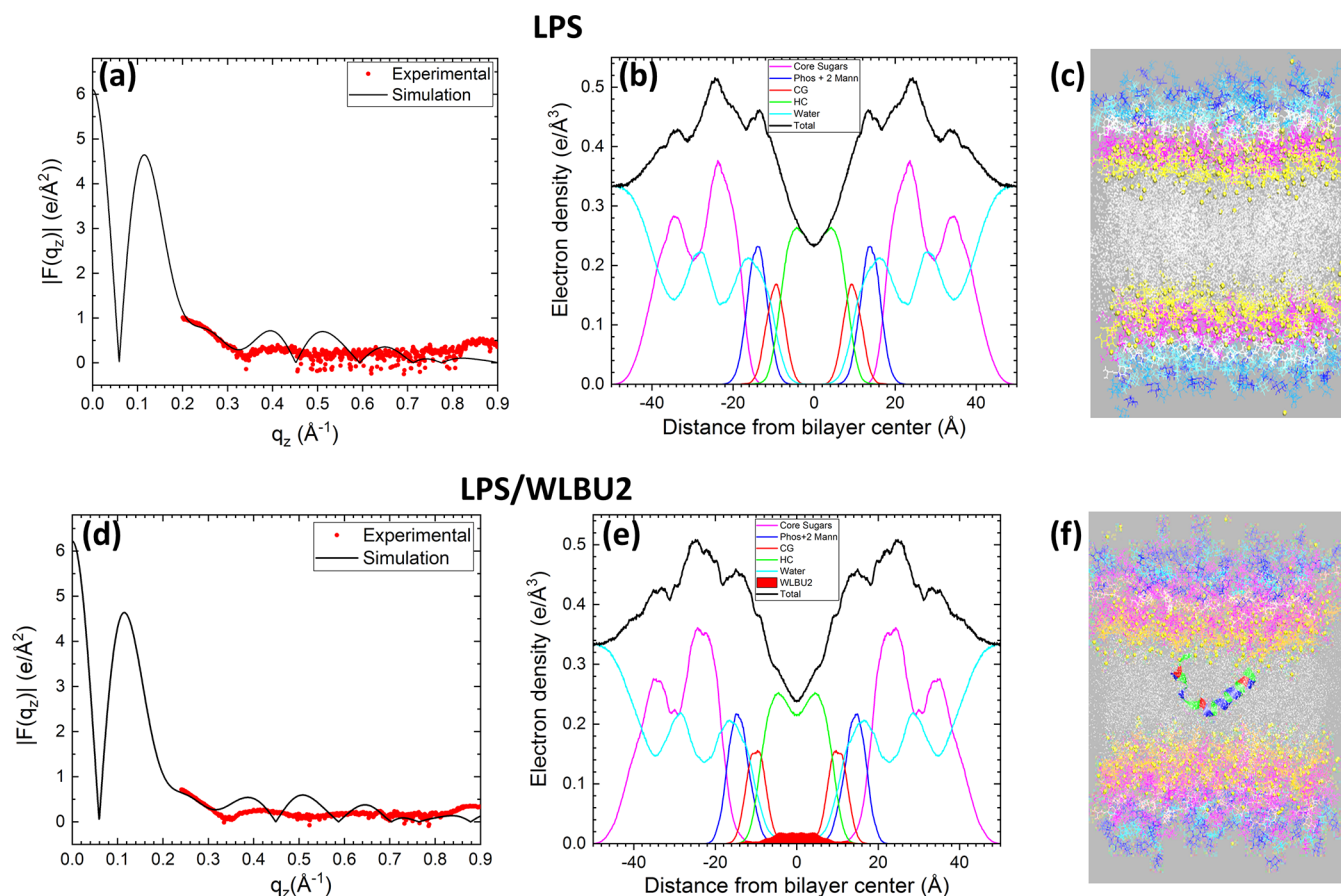


Figure 11. (a) LPS simulated (black line) and experimental form factors (red circles). (b) LPS simulated EDP. Colors: Total, black; core sugars, magenta; phosphate + two mannose residues, blue; carbonyl-glycerol, red; hydrocarbon, green; and water, cyan. (c) VMD visualization of LPS control. Colors: Na^+ ions, yellow; two mannose residues, magenta; phosphate groups, white; core sugars, cyan and blue; and hydrocarbon chains, light gray. (d) LPS/WLBU2, simulated (black line) and experimental form factors (red circles). (e) LPS/WLBU2 simulated EDP. (f) VMD visualization of LPS/WLBU2. Colors: as in 11(c). Colors in WLBU2: R, green; V, blue; and W, red.

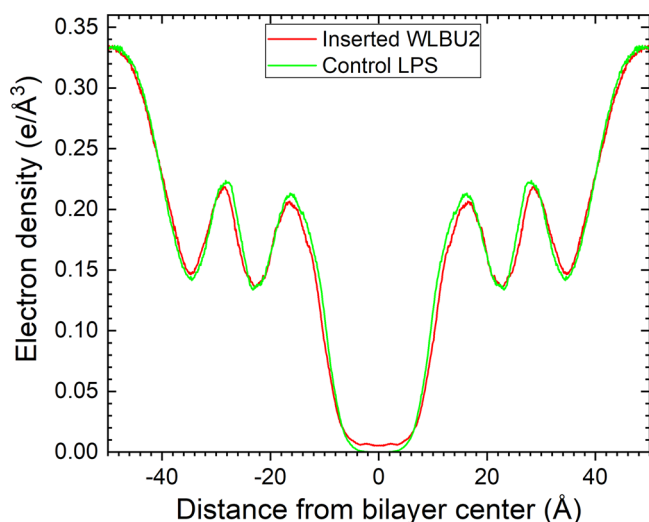


Figure 12. Electron density of water in control LPS (green) and in LPS:WLBU2 75:1 (red).

location would facilitate self-promoted uptake⁵⁹ of WLBU2 through the outer membrane that must occur for it to reach the inner membrane. When the highly positively charged arginine residues embed deep into the hydrocarbon phase, they cause water to enter. This is shown in Figure 12, where there is a

Table 2. Summary of Area Per Lipid and Membrane Hydrocarbon Thickness

lipid system	surface tension (dyne/cm)	APL (\AA^2)	$2D_C$ (\AA)
KDO2 control ($-6e$)	0	160.3 ± 0.9	25.4 ± 0.2
[KDO2 control ($-4e$)]	0	172.8 ± 2.3	24.0 ± 0.2
KDO2/WLBU2 ($-4e$)	0	171.3 ± 2.0	24.5 ± 0.2
G(-) control	9	70.4 ± 1.2	29.6 ± 0.2
G(-)/WLBU2 ^a	11	74.9 ± 0.2	29.0 ± 0.2
G(+) control	0	70.2 ± 1.7	29.0 ± 0.2
G(+)/WLBU2 ^b	12	80.9 ± 2.8	28.1 ± 0.2
[LPS ($-10e$)]	0	176.7 ± 1.0	18.6 ± 0.2
LPS ($-8e$)	0	179.6 ± 0.6	18.0 ± 0.2
LPS/WLBU2 ($-8e$)	0	178.9 ± 1.1	18.2 ± 0.2

^a87.4 G(-) lipids:1 WLBU2, combined surface tension 11.2 dyne/cm. ^bcombined 11.8 dyne/cm. Simulated samples italicized in brackets [] had a poorer agreement with experimental data as determined by the chi-square in the SimtoExp program. Areas per lipid were calculated from the final 100 ns of the simulation as described in the Materials and Methods section. Hydrocarbon bilayer thicknesses ($2D_C$) were estimated from the Gibbs dividing surface of the lipid chain region in the EDP from the simulation.

significant electron density of water at the center of the bilayer with embedded WLBU2 in LPS. Therefore, in the first step of

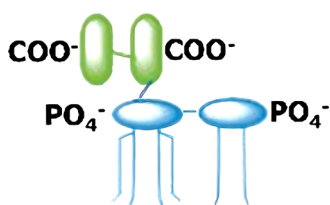


Figure 13. Cartoon structure of KDO2. Colors: octulosonic acid residues, green ellipsoids; mannose residues, blue ellipsoids.

bacterial killing as WLBU2 encounters the negatively charged bacterial membrane, we suggest it binds to the carboxyl groups on the octulosonic acid residues and then penetrates into the hydrocarbon interior with accompanying water due to the considerable membrane fluctuations.

Traditionally, the outer membrane (OM) has been thought of as the major permeability barrier to antibiotics. Conventional antibiotics such as β -lactams are thought to enter the OM through pores formed by porin proteins,⁶⁰ but generally, only hydrophilic substances less than 600 Daltons can diffuse through the porins. In addition, the OM has an unusually low permeability to hydrophobic molecules,⁶¹ while cationic AMPs, like WLBU2, are able to permeate the OM similarly to cell-penetrating peptides due to their interaction with negatively charged lipid headgroups.⁶² The simulation visualization in Figure 11f shows that two of the Rs are closer to the interfacial region, while the remaining Rs, Vs, and Ws are equally present at all depths in the hydrocarbon region. The location of Rs close to the interface may be important in drawing water into the membrane, and the bent conformation would naturally occur in this thin hydrocarbon interior.

Although our study did not address the next step, presumably WLBU2 then exits the OM and enters the periplasmic space. The periplasm has many functions, including protein secretion and folding, environmental sensing, peptidoglycan synthesis, osmoregulation, resistance to turgor pressure, and sensing and resistance to cationic antimicrobial peptides.⁶³ Within the periplasmic space is a layer of crosslinked sugars and amino acids termed peptidoglycan, which is linked to the outer membrane through covalent linkages to the outer membrane lipoprotein. Multicomponent protein complexes such as the flagellar machine span the two membranes. Due to its constituents, the periplasmic space is osmotically active. A Donnan equilibrium controls the flow of water and ions from the cytoplasm, or from the extracellular fluid, to the periplasm⁶² and it is generally thought that the gel-like periplasm is fairly permeable to small molecules like antibiotics and AMPs.⁶²

For G(−) bacteria, the AMPs next encounter the inner membrane (IM). Our NR results revealed in Figure S5b that the bent conformation of WLBU2 finds two locations in the IM: 63% in the headgroup and 37% in the hydrocarbon interior (see also Figure S7a). This dual location may be important for WLBU2's function of perturbing the membrane and killing the bacteria. In the surface states, Figure 8 shows that R spans the range from 11 to 30 Å, V spans 12 to 26 Å, and W spans 6 to 23 Å from the bilayer center. The outermost position for R is consistent with its smallest hydrophobicity.³⁴ R extends to the bulk water phase and is in position to bind to both the phosphate headgroup of the G(−) LMM near 20 Å and the carbonyl-glycerol near 16 Å from the bilayer center (see Figure 8b). In the inserted state, R spans a region from the headgroup in the proximal monolayer to the hydrocarbon edge in the distal

monolayer. Thus, even when R is in the hydrocarbon region, it has a portion that can bind to the phosphate headgroup. This electrostatic binding must be crucial in anchoring WLBU2 to the lipid headgroup region in the G(−) inner membrane while still penetrating deep into the hydrocarbon region. W has a component at the bilayer carbonyl-glycerol interfacial region at 14 Å when in both the surface and inserted states, which is a second anchor that keeps WLBU2 from fully penetrating the hydrocarbon interior.

G(+) membrane/WLBU2 interaction is similar to that of the G(−) membrane, which is reasonable since WLBU2 kills both types of bacteria efficiently.¹⁶ Our NR results revealed in Figure 5c that the bent conformation of WLBU2 finds two locations in G(+): 54% in the headgroup and 46% in the hydrocarbon interior. One difference compared to the G(−) membrane is that the headgroup and hydrocarbon positions of WLBU2 are more separated in G(+) (compare Figure 10c to Figure 8a), but R in the bent surface state in G(+) is again aligned at the phosphate position near 20 Å from the bilayer center. W is again aligned with the interfacial region at \sim 15 Å from the bilayer center. When WLBU2 is in the bilayer interior, R overlaps with the surface R state, thus forming a continuous positive charge across the bilayer. The smaller Vs follow the positions of Rs and Ws. The continuous line of positive charges allows water to enter the hydrocarbon interior creating a pathway for water and ions to leave the bacterial cell, thereby killing it.

In this work, we have not explored the question of AMP aggregation and how aggregated WLBU2s might interact with the bacterial membrane. A role for aggregation in selectivity between a eukaryotic and bacterial membrane model was investigated for the fungicide fengycin⁶⁴ at a much higher lipid:peptide molar ratio than in this work since we constrained our peptide concentration to the highest permissible in the XDS experiment (76:1). In addition, fengycin contains a lipophilic tail, which could cause aggregation via van der Waals attractive interactions. Similarly in a study of the AMP polymyxin E (colistin) on planar lipid bilayers composed of LPS/PC, it was found that colistin, which also contains a lipophilic tail, induces large-scale clustering as it segregates out LPS.⁶⁵ Since WLBU2 is highly positively charged (+13 e), it is unlikely that self-aggregation would occur, even when binding to phosphate headgroups. We did explore the difference in adding WLBU2 on both sides of G(−) IM compared to only one side and found that this caused little difference in the form factors (see Figure S8). In addition, we have not yet used MD simulation to explore the interaction of WLBU2 with an LMM of the host eukaryotic membrane that contains phosphatidylcholine, phosphatidylethanolamine, sphingomyelin, and cholesterol.

To summarize, this work reports on the use of neutron and X-ray diffuse scattering to shorten the time required for all-atom MD simulations of the AMP WLBU2 interacting with bacterial LMMs. By constraining the thickness of the simulated membrane using a surface tension to match that obtained by XDS experiments, and by constraining the location of the peptide in the membrane to match that obtained by NR, micro-, or millisecond simulations are not required. Importantly, constraints on peptide location are finally removed, allowing equilibration. One important molecular result in this investigation is the observation of water at the center of the bilayer when WLBU2 is in the inserted state. Other investigations of the KvAP voltage-gated potassium channel^{45,66} and the HIV Tat protein⁶⁷ have also found water with charged amino acid residues and phosphate groups that are buried in the

hydrocarbon interior. In the case of WLBU2, the internal water is continuous with the headgroup water due to a dual anchoring of WLBU2 in the headgroup and in the interfacial region and also penetration into the hydrocarbon interior. Arginine's binding to phosphate residues plus tryptophan's location near the bilayer interface may be important anchoring mechanisms. WLBU2 causes a small (~ 1 Å) thinning at a lipid:peptide molar ratio of $\sim 76:1$ in both G(−) and G(+) LMMs. An increase in APL with the addition of WLBU2 is also observed for G(−) and G(+) LMMs. Thus, the dual location of WLBU2 in the headgroup and hydrocarbon regions, the presence of water, phosphates, and ions in the interior, the location of arginines at the phosphate, tryptophans at the interfacial region, and the slight bilayer thinning all contribute to membrane destabilization thus leading to bacterial killing.

■ ASSOCIATED CONTENT

SI Supporting Information

The Supporting Information is available free of charge at <https://pubs.acs.org/doi/10.1021/acs.jpcb.2c03193>.

Materials and Methods and Results for KDO2 simulations, MD stability tests, NR and XDS in Figures S1–S8 (PDF)

Accession Codes

The structures in this work were deposited in the Small Angle Scattering Biological Data Bank (SASBDB) on January 17, 2022. Their #s are SASDNU4, SASDNV4, SASDNW4, SASDNX4, SASDNY4, SASDNZ4, SASDN25, and SASDN35. They will “go live” upon publication of this paper.

■ AUTHOR INFORMATION

Corresponding Authors

Jeffery B. Klauda – Department of Chemical and Biomolecular Engineering, University of Maryland, College Park, Maryland 20742, United States; orcid.org/0000-0001-8725-1870; Phone: 301-314-9126; Email: jbklauda@umd.edu; Fax: 301-314-9126

James C. Gumbart – School of Physics, Georgia Institute of Technology, Atlanta, Georgia 30332, United States; orcid.org/0000-0002-1510-7842; Phone: 404-385-0797; Email: gumbart@physics.gatech.edu; Fax: 404-894-9958

Stephanie Tristram-Nagle – Biological Physics Group, Physics Department, Carnegie Mellon University, Pittsburgh, Pennsylvania 15213, United States; orcid.org/0000-0003-2271-7056; Phone: 412-268-3174; Email: stn@cmu.edu; Fax: 412-681-0648

Authors

Robert Allsopp – Department of Chemical and Biomolecular Engineering, University of Maryland, College Park, Maryland 20742, United States

Anna Pavlova – School of Physics, Georgia Institute of Technology, Atlanta, Georgia 30332, United States

Tyler Cline – Department of Chemical and Biomolecular Engineering, University of Maryland, College Park, Maryland 20742, United States

Aria M. Salyapongse – Biological Physics Group, Physics Department, Carnegie Mellon University, Pittsburgh, Pennsylvania 15213, United States

Richard E. Gillilan – Cornell High Energy Synchrotron Source (CHESS), Cornell University, Ithaca, New York 14853, United States

Y. Peter Di – Department of Environmental and Occupational Health, University of Pittsburgh, Pittsburgh, Pennsylvania 15260, United States; orcid.org/0000-0003-2028-2087

Berthony Deslouches – Department of Environmental and Occupational Health, University of Pittsburgh, Pittsburgh, Pennsylvania 15260, United States

Complete contact information is available at:

<https://pubs.acs.org/10.1021/acs.jpcb.2c03193>

Author Contributions

R.A., A.P., and T.C.: Software, Visualization, Formal analysis, and Methodology; J.K., J.C.G.: Data curation, Funding acquisition, Resources, and Supervision; A.M.S.: Formal analysis; R.E.G.: Investigation; Y.P.D., B.D.: Writing, review, and editing; and S.T.-N.: Conceptualization, Validation, Investigation, Formal analysis, Data curation, Writing the original draft, Supervision, Project Administration, and Funding acquisition.

Notes

The authors declare no competing financial interest.

■ ACKNOWLEDGMENTS

This work is based upon research conducted at Carnegie Mellon University and at the Center for High Energy X-ray Sciences (CHEXS), which is supported by the National Science Foundation under award DMR-1829070, and the Macromolecular Diffraction at the Cornell High Energy Synchrotron Sources (CHESS) (MacCHESS) facility, which is supported by award 1-P30-GM124166-01A1 from the National Institute of General Medical Sciences, National Institutes of Health, and New York State's Empire State Development Corporation (NYSTAR). The authors would like to thank Drs. Irina Kriksunov and Qingqiu Huang for help with the virtual data collection at CHESS beamline ID7A1 and Dr. John Nagle for useful discussions. Additional support for this work was from Carnegie Mellon SURF (A.S.), National Institutes of Health (NIH) R01AI133351 (Y.P.D., S.T.N.), NIH R01GM125917 (B.D., S.T.N.), NIH R01GM123169 (J.C.G., A.P.), National Science Foundation (NSF) MCB-2115790 (S.T.N.), and NSF MCB-1951425 (J.K., R.A.). Simulations were performed on the Extreme Science and Engineering Discovery Environment (XSEDE) supercomputers, which are supported by NSF grant ACI-1548562, under allocations MCB-100139 and MCB-130183, and on Comet and Expanse at the San Diego Supercomputer Center at U.C. San Diego.

■ ABBREVIATIONS USED

AA, all-atom; APL, area per lipid; ATR-FTIR, attenuated total reflection-Fourier transform infrared spectroscopy; AMP, antimicrobial peptide; CHESS, Cornell High Energy Synchrotron Source; CD, circular dichroism; CPP, cell-penetrating peptide; DLPG, 1,2-dilauroyl-*sn*-glycero-3-phospho-(1'-*rac*-glycerol); DOTAP, 1,2-dioleoyl-3-trimethylammonium-propane (chloride salt); EDP, electron density profile; G(−), Gram-negative; G(+), Gram-positive; HIP, hexafluoroisopropanol; IM, inner membrane; K⁺, potassium ions; KDO2, 3-deoxy-D-manno-octulosonic acid; (LMMs), lipid model membranes; LPS, lipopolysaccharide; Na⁺, sodium ions; NMR, nuclear magnetic resonance; NR, neutron reflectivity; OM, outer membrane; PBS, phosphate-buffered saline; POPE, 1-palmitoyl-2-oleoyl-*sn*-glycero-3-phosphoethanolamine; POPG, 1-palmitoyl-2-oleoyl-*sn*-glycero-3-phospho-(10-*rac*-glycerol)

sodium salt; R, arginine; SAXS, small-angle X-ray scattering; SFG, sum frequency generation; TOCL, 10,30-bis-[1,2-dioleoyl-*sn*-glycero-3-phospho]-*sn*-glycerol sodium salt; V, valine; W, tryptophan; XDS, X-ray diffuse scattering

REFERENCES

- (1) WHO. Antimicrobial Resistance WHO Global Report on Surveillance, 2014, <http://www.who.int/drugresistance/documents/surveillancereport/en/>.
- (2) O'Niell, J. *Tackling Drug-resistant Infections Globally: Final Report and Recommendations*; United Kingdom, 2016; pp 1–84.
- (3) Dürr, U. H.; Sudheendra, U. S.; Ramamoorthy, A. LL-37, the only human member of the cathelicidin family of antimicrobial peptides. *Biochim. Biophys. Acta, Biomembr.* **2006**, *1758*, 1408–1425.
- (4) Deslouches, B.; Islam, K.; Craig, J. K.; Paranjape, S. M.; Montelaro, R. C.; Mietzner, T. A. Activity of the de novo engineered antimicrobial peptide WLBU2 against *Pseudomonas aeruginosa* in human serum and whole blood: implications for systemic applications. *Antimicrob. Agents Chemother.* **2005**, *49*, 3208–3216.
- (5) Tencza, S. B.; Creighton, D. J.; Yuan, T.; Vogel, H. J.; Montelaro, R. C.; Mietzner, T. A. Lentivirus-derived antimicrobial peptides: increased potency by sequence engineering and dimerization. *J. Antimicrob. Chemother.* **1999**, *44*, 33–41.
- (6) Lohner, K. The Role of Membrane Lipid Composition in Cell Targeting of Antimicrobial Peptides. In *Development of Novel Antimicrobial Agents: Emerging Strategies*, Lohner, K., Ed.; Horizon Scientific Press, 2001; pp 149–165.
- (7) Deslouches, B.; Gonzalez, I. A.; DeAlmeida, D.; Islam, K.; Steele, C.; Montelaro, R. C.; Mietzner, T. A. De novo-derived cationic antimicrobial peptide activity in a murine model of *Pseudomonas aeruginosa* bacteraemia. *J. Antimicrob. Chemother.* **2007**, *60*, 669–672.
- (8) Chen, C.; Deslouches, B.; Montelaro, R. C.; Di, Y. P. Enhanced efficacy of the engineered antimicrobial peptide WLBU2 via direct airway delivery in a murine model of *Pseudomonas aeruginosa* pneumonia. *Clin. Microbiol. Infect.* **2018**, *24*, S47.e1.
- (9) Deslouches, B.; Steckbeck, J. D.; Craig, J. K.; Doi, Y.; Mietzner, T. A.; Montelaro, R. C. Rational design of engineered cationic antimicrobial peptides consisting exclusively of arginine and tryptophan, and their activity against multidrug-resistant pathogens. *Antimicrob. Agents Chemother.* **2013**, *57*, 2511–2521.
- (10) Steckbeck, J. D.; Deslouches, B.; Montelaro, R. C. Antimicrobial peptides: new drugs for bad bugs? *Expert Opin. Biol. Ther.* **2014**, *14*, 11–14.
- (11) Lashua, L. P.; Melvin, J. A.; Deslouches, B.; Pilewski, J. M.; Montelaro, R. C.; Bomberger, J. M. Engineered cationic antimicrobial peptide (eCAP) prevents *Pseudomonas aeruginosa* biofilm growth on airway epithelial cells. *J. Antimicrob. Chemother.* **2016**, *71*, 2200–2207.
- (12) Deslouches, B.; Steckbeck, J. D.; Craig, J. K.; Doi, Y.; Burns, J. L.; Montelaro, R. C. Engineered cationic antimicrobial peptides to overcome multidrug resistance by ESKAPE pathogens. *Antimicrob. Agents Chemother.* **2015**, *59*, 1329–1333.
- (13) Deslouches, B.; Phadke, S. M.; Lazarevic, V.; Cascio, M.; Islam, K.; Montelaro, R. C.; Mietzner, T. A. De novo generation of cationic antimicrobial peptides: influence of length and tryptophan substitution on antimicrobial activity. *Antimicrob. Agents Chemother.* **2005**, *49*, 316–322.
- (14) Di, Y. P.; Lin, Q.; Chen, C.; Montelaro, R. C.; Doi, Y.; Deslouches, B. Enhanced therapeutic index of an antimicrobial peptide in mice by increasing safety and activity against multidrug-resistant bacteria. *Sci. Adv.* **2020**, *6*, eaay6817.
- (15) Huang, D.; Dobbins, D.; Ghahramani, P.; Friedland, I.; Steckbeck, J. A phase 1 study of safety, tolerability and pharmacokinetics of single ascending doses of a first in human engineered cationic peptides, PLG0206, intravenously administered in healthy subjects. *Antimicrob. Agents Chemother.* **2022**, *66*, 296–305.
- (16) Heinrich, F.; Salyapongse, A.; Kumagai, A.; Dupuy, F. G.; Shukla, K.; Penk, A.; Huster, D.; Ernst, R. K.; Pavlova, A.; Gumbart, J. C.; Deslouches, B.; Di, Y. P.; Tristram-Nagle, S. Synergistic biophysical techniques reveal structural mechanisms of engineered cationic antimicrobial peptides in lipid model membranes. *Chem. - Eur. J.* **2020**, *26*, 6247–6256.
- (17) Ratledge, C.; Wilkinson, S. G. *Microbial Lipids*; Academic Press: London; San Diego, 1988; p 1.
- (18) Durell, S. R.; Brooks, B. R.; Bennaim, A. Solvent-induced forces between two hydrophilic groups. *J. Phys. Chem. A* **1994**, *98*, 2198–2202.
- (19) Klauda, J. B.; Kucerka, N.; Brooks, B. R.; Pastor, R. W.; Nagle, J. F. Simulation-based methods for interpreting X-ray data from lipid bilayers. *Biophys. J.* **2006**, *90*, 2796–2807.
- (20) Phillips, J. C.; Hardy, D. J.; Maia, J. D. C.; Stone, J. E.; Ribeiro, J. V.; Bernardi, R. C.; Tajkhorshid, E.; et al. Scalable molecular dynamics on CPU and GPU architectures with NAMD. *J. Chem. Phys.* **2020**, *153*, No. 044130.
- (21) Klauda, J. B.; Venable, R. M.; Freites, J. A.; O'Connor, J. W.; Tobias, D. J.; Mondragon-Ramirez, C.; Pastor, R. W.; et al. Update of the CHARMM all-atom additive force field for lipids: Validation on six lipid types. *J. Phys. Chem. B* **2010**, *114*, 7830–7843.
- (22) Huang, J.; Rauscher, S.; Nawrocki, G.; Ran, T.; Feig, M.; de Groot, B. L.; Grubmüller, H.; MacKerell, A. D. CHARMM36m: an improved force field for folded and intrinsically disordered proteins. *Nat. Methods* **2017**, *14*, 71–73.
- (23) Darden, T.; York, D.; Pedersen, L. Particle mesh Ewald - an $N \log(N)$ method for Ewald sums in large systems. *J. Chem. Phys.* **1993**, *98*, 10089–10092.
- (24) Jo, S.; Kim, T.; Iyer, V. G.; Im, W. CHARMM-GUI: a web-based graphical user interface for CHARMM. *J. Comput. Chem.* **2008**, *29*, 1859–1865.
- (25) Wu, E. L.; Cheng, X.; Jo, S.; Rui, H.; Song, K. C.; Davila-Contreras, E. M.; Im, W.; et al. CHARMM-GUI membrane builder toward realistic biological membrane simulations. *J. Comput. Chem.* **2014**, *35*, 1997–2004.
- (26) Rice, A.; Rooney, M. T.; Greenwood, A. I.; Cotten, M. L.; Wereszczynski, J. Lipopolysaccharide simulations are sensitive to phosphate charge and ion parameterization. *J. Chem. Theory Comput.* **2020**, *16*, 1806–1815.
- (27) Kučerka, N.; Katsaras, J.; Nagle, J. F. Comparing membrane simulations to scattering experiments: Introducing the SIMtoEXP software. *J. Membrane Biol.* **2010**, *235*, 43–50.
- (28) Raman, S.; Vernon, R.; Thompson, J.; Tyka, M.; Sadreyev, R.; Pei, J. M.; Baker, D.; et al. Structure prediction for CASP8 with all-atom refinement using Rosetta. *Proteins* **2009**, *77*, 89–99.
- (29) Song, Y. F.; DiMaio, F.; Wang, R. Y. R.; Kim, D.; Miles, C.; Brunette, T. J.; Thompson, J.; Baker, D. High-resolution comparative modeling with RosettaCM. *Structure* **2013**, *21*, 1735–1742.
- (30) Jo, S.; Cheng, X.; Lee, J.; Kim, S.; Park, S. J.; Patel, D. S.; Im, W.; et al. CHARMM-GUI 10 years for biomolecular modeling and simulation. *J. Comput. Chem.* **2017**, *38*, 1114–1124.
- (31) Lee, J.; Patel, D. S.; Stahle, J.; Park, S. J.; Kern, N. R.; Kim, S.; Im, W.; et al. CHARMM-GUI membrane builder for complex biological membrane simulations with glycolipids and lipoglycans. *J. Chem. Theory Comput.* **2019**, *15*, 775–786.
- (32) Loney, R. W.; Panzuela, S.; Chen, J.; Yang, Z.; Fritz, J. R.; Dell, Z.; Corradi, V.; Kumar, K.; Tieleman, D. P.; Hall, S. B.; Tristram-Nagle, S. A. Location of the hydrophobic surfactant proteins, SP-B and SP-C, in fluid-phase bilayers. *Journal of Physical Chemistry B* **2020**, *124*, 6763–6774.
- (33) Petrache, H. I.; Feller, S. E.; Nagle, J. F. Determination of component volumes of lipid bilayers from simulations. *Biophys. J.* **1997**, *72*, 2237–2242.
- (34) Wimley, W. C.; White, S. H. Experimentally determined hydrophobicity scale for proteins at membrane interfaces. *Nat. Struct. Biol.* **1996**, *3*, 842–848.
- (35) Deserno, M. Mesoscopic membrane physics: concepts, simulations, and selected applications. *Macromol. Rapid Commun.* **2009**, *30*, 752–771.
- (36) Wassenaar, T. A.; Pluhackova, K.; Bockmann, R. A.; Marrink, S. J.; Tieleman, D. P. Going backward: A flexible geometric approach to

- reverse transformation from coarse grained to atomistic models. *J. Chem. Theory Comput.* **2014**, *10*, 676–690.
- (37) Monticelli, L.; Kandasamy, S. K.; Periole, X.; Larson, R. G.; Tieleman, D. P.; Marrink, S. J. The MARTINI Coarse-Grained Force Field: Extension to Proteins. *J. Chem. Theory Comput.* **2008**, *4*, 819–834.
- (38) Rzepiela, A. J.; Schafer, L. V.; Goga, N.; Risselada, H. J.; De Vries, A. H.; Marrink, S. J. Reconstruction of atomistic details from coarse-grained structures. *J. Comput. Chem.* **2010**, *31*, 1333–1343.
- (39) Rzepiela, A. J.; Sengupta, D.; Goga, N.; Marrink, S. J. Membrane poration by antimicrobial peptides combining atomistic and coarse-grained descriptions. *Faraday Discuss* **2010**, *144*, 431–443.
- (40) Lyubartsev, A. P. Multiscale modeling of lipids and lipid bilayers. *Eur. Biophys. J.* **2005**, *35*, 53–61.
- (41) Marrink, S. J.; Tieleman, D. P. Perspective on the Martini model. *Chem. Soc. Rev.* **2013**, *42*, 6801–6822.
- (42) Wang, Z. J.; Deserno, M. A Systematically Coarse-Grained Solvent-Free Model for Quantitative Phospholipid Bilayer Simulations. *J. Phys. Chem. B* **2010**, *114*, 11207–11220.
- (43) Pluhackova, K.; Bockmann, R. A. Biomembranes in atomistic and coarse-grained simulations. *J. Phys.: Condens. Matter* **2015**, *27*, 323103.
- (44) Esteban-Martin, S.; Salgado, J. Self-assembling of peptide/membrane complexes by atomistic molecular dynamics simulations. *Biophys. J.* **2007**, *92*, 903–912.
- (45) Monticelli, L.; Robertson, K. M.; MacCallum, J. L.; Tieleman, D. P. Computer simulation of the KvAP voltage-gated potassium channel: steered molecular dynamics of the voltage sensor. *FEBS Lett.* **2004**, *564*, 325–332.
- (46) Henriques, J.; Cragnell, C.; Skepo, M. Molecular dynamics simulations of intrinsically disordered proteins: Force field evaluation and comparison with experiment. *J. Chem. Theory Comput.* **2015**, *11*, 3420–3431.
- (47) Jang, H.; Connelly, L.; Arce, F. T.; Ramachandran, S.; Kagan, B. L.; Lal, R.; Nussinov, R. Mechanisms for the insertion of toxic, fibril-like beta-amyloid oligomers into the membrane. *J. Chem. Theory Comput.* **2013**, *9*, 822–833.
- (48) Isaksson, J.; Brandsdal, B. O.; Engqvist, M.; Flaten, G. E.; Svendsen, J. S. M.; Stensen, W. A synthetic antimicrobial peptidomimetic (LTX 109): Stereochemical impact on membrane disruption. *J. Med. Chem.* **2011**, *54*, 5786–5795.
- (49) Sforça, M. L.; Oyama, S.; Canduri, F.; Lorenzi, C. C. B.; Pertinhez, T. A.; Konno, K.; Spisni, A.; et al. How C-terminal carboxyamidation alters the biological activity of peptides from the venom of the eumenine solitary wasp. *Biochemistry* **2004**, *43*, 5608–5617.
- (50) Ho, S. W.; Jung, D.; Calhoun, J. R.; Lear, J. D.; Okon, M.; Scott, W. R. P.; Hancock, R. E. W.; Straus, S. K. Effect of divalent cations on the structure of the antibiotic daptomycin. *Eur. Biophys. J.* **2008**, *37*, 421–433.
- (51) Ding, B.; Jasensky, J.; Li, Y. X.; Chen, Z. Engineering and characterization of peptides and proteins at surfaces and interfaces: A case study in surface-sensitive vibrational spectroscopy. *Acc. Chem. Res.* **2016**, *49*, 1149–1157.
- (52) Orioni, B.; Bocchinfuso, G.; Kim, J. Y.; Palleschi, A.; Grande, G.; Bobone, S.; Stella, L.; et al. Membrane perturbation by the antimicrobial peptide PMAP-23: A fluorescence and molecular dynamics study. *Biochim. Biophys. Acta, Biomembr.* **2009**, *1788*, 1523–1533.
- (53) Kaur, K.; Andrew, L. C.; Wishart, D. S.; Vederas, J. C. Dynamic relationships among type IIa bacteriocins: Temperature effects on antimicrobial activity and on structure of the C-terminal amphipathic alpha helix as a receptor-binding region. *Biochemistry* **2004**, *43*, 9009–9020.
- (54) Kumagai, A.; Dupuy, F. G.; Arsov, Z.; Elhady, Y.; Moody, D.; Ernst, R. K.; Tristram-Nagle, S.; et al. Elastic behavior of model membranes with antimicrobial peptides depends on lipid specificity and D-enantiomers. *Soft Matter* **2019**, *15*, 1860–1868.
- (55) Rodriguez, J. R.; Garcia, A. E. Concentration dependence of NaCl ion distributions around DPPC lipid bilayers. *Interdiscip. Sci.: Comput. Life Sci.* **2011**, *3*, 272–282.
- (56) Mukherjee, S.; Kar, R. K.; Nanga, R. P. R.; Mroue, K. H.; Ramamoorthy, A.; Bhunia, A. Accelerated molecular dynamics simulation analysis of MSI-594 in a lipid bilayer. *Phys. Chem. Chem. Phys.* **2017**, *19*, 19289–19299.
- (57) Delcour, A. H. Outer membrane permeability and antibiotic resistance. *Biochim. Biophys. Acta, Proteins Proteomics* **2009**, *1794*, 808–816.
- (58) Dupuy, F. G.; Pagano, I.; Andenoro, K.; Peralta, M. F.; Elhady, Y.; Heinrich, F.; Tristram-Nagle, S. Selective interaction of colistin with lipid model membranes. *Biophys. J.* **2018**, *114*, 919–928.
- (59) Hancock, R. E. W. Alterations in outer membrane permeability. *Annu. Rev. Microbiol.* **1984**, *38*, 237–264.
- (60) James, C. E.; Mahendran, K. R.; Molitor, A.; Bolla, J. M.; Bessonov, A. N.; Winterhalter, M.; Page, J. M. How beta-lactam antibiotics enter bacteria: A dialogue with the porins. *PLoS One* **2009**, *4*, e5453.
- (61) Nikaido, H. Outer membrane of Salmonella-typhimurium transmembrane diffusion of some hydrophobic substances. *Biochim. Biophys. Acta* **1976**, *433*, 118–132.
- (62) Thorén, P. E.; Persson, D.; Karlsson, M.; Norden, B. The Antennapedia peptide penetratin translocates across lipid bilayers - the first direct observation. *FEBS Lett.* **2000**, *482*, 265–268.
- (63) Miller, S. I.; Salama, N. R.; The gram-negative bacterial periplasm: Size matters. *PLoS Biol.* **2018**, *16*, DOI: 10.1371/journal.pbio.2004935.
- (64) Sur, S.; Romo, T. D.; Grossfield, A. Selectivity and mechanism of fengycin, an antimicrobial lipopeptide, from molecular dynamics. *J. Phys. Chem. B* **2018**, *122*, 2219–2226.
- (65) Khadka, N. K.; Aryal, C. M.; Pan, J. J. Lipopolysaccharide-dependent membrane permeation and lipid clustering caused by cyclic lipopeptide colistin. *ACS Omega* **2018**, *3*, 17828–17834.
- (66) Freitas, J. A.; Tobias, D. J.; von Heijne, G.; White, S. H. Interface connections of a transmembrane voltage sensor. *Proc. Natl. Acad. Sci. U.S.A.* **2005**, *102*, 15059–15064.
- (67) Neale, C.; Huang, K.; Garcia, A. E.; Tristram-Nagle, S. Penetration of HIV-1 Tat47-57 into PC/PE bilayers assessed by MD simulation and X-ray scattering. *Membranes* **2015**, *5*, 473–494.